

Quantum frequency conversion of quantum memory compatible photons to telecommunication wavelengths

Xavier Fernandez-Gonzalvo,^{1,2} Giacomo Corrielli,^{1,3} Boris Albrecht,¹ Marcel.li Grimaù,^{1,4} Matteo Cristiani,^{1*} and Hugues de Riedmatten^{1,5}

¹ *ICFO-Institut de Ciències Fòniques, Mediterranean Technology Park, 08860 Castelldefels (Barcelona), Spain.*

² *Current address: Department of Physics, University of Otago, 730 Cumberland Street, 9016 Dunedin, New Zealand*

³ *Current address: Politecnico di Milano, Dipartimento di Fisica - Piazza Leonardo da Vinci, 32, I-20133 Milano, Italy*

⁴ *Current address: Institute for Quantum Information Science and Department of Physics and Astronomy, University of Calgary, Calgary, Alberta T2N 1N4, Canada*

⁵ *ICREA-Institució Catalana de Recerca i Estudis Avançats, 08015 Barcelona, Spain*

[*matteo.cristiani@icfo.es](mailto:matteo.cristiani@icfo.es)

Abstract: We report an experiment demonstrating quantum frequency conversion of weak light pulses compatible with atomic quantum memories to telecommunication wavelengths. We use a PPLN nonlinear waveguide to convert weak coherent states at the single photon level with a duration of 30ns from a wavelength of 780nm to 1552nm. We measure a maximal waveguide internal (external) conversion efficiency $\eta_{int} = 0.41$ ($\eta_{ext} = 0.25$), and we show that the signal to noise ratio (*SNR*) is good enough to reduce the input photon number below 1. In addition, we show that the noise generated by the pump beam in the crystal is proportional to the spectral bandwidth of the device, suggesting that narrower filtering could significantly increase the *SNR*. Finally, we demonstrate that the quantum frequency converter can operate in the quantum regime by converting a time-bin qubit and measuring the qubit fidelity after conversion.

© 2021 Optical Society of America

OCIS codes: (270.0270) Quantum optics; (190.4223) Nonlinear wave mixing; (270.5585) Quantum information and processing; (270.5565) Quantum communications.

References and links

1. H.-J. Briegel, W. Dür, J. I. Cirac, and P. Zoller, "Quantum repeaters: The role of imperfect local operations in quantum communication," *Phys. Rev. Lett.* **81**, 5932–5935 (1998).
2. L.-M. Duan, M. D. Lukin, J. I. Cirac, and P. Zoller, "Long-distance quantum communication with atomic ensembles and linear optics," *Nature* **414**, 413–418 (2001).
3. N. Sangouard, C. Simon, H. de Riedmatten, and N. Gisin, "Quantum repeaters based on atomic ensembles and linear optics," *Rev. Mod. Phys.* **83**, 33–80 (2011).
4. C. W. Chou, H. de Riedmatten, D. Felinto, S. V. Polyakov, S. J. van Enk, and H. J. Kimble, "Measurement-induced entanglement for excitation stored in remote atomic ensembles," *Nature* **438**, 828–832 (2005).
5. Z.-S. Yuan, Y.-A. Chen, B. Zhao, S. Chen, J. Schmiedmayer, and J.-W. Pan, "Experimental demonstration of a bdcz quantum repeater node," *Nature* **454**, 1098–1101 (2008).
6. B. Lauritzen, J. Minář, H. de Riedmatten, M. Afzelius, N. Sangouard, C. Simon, and N. Gisin, "Telecommunication-wavelength solid-state memory at the single photon level," *Phys. Rev. Lett.* **104**, 080502–(2010).

7. B. Lauritzen, J. Minář, H. de Riedmatten, M. Afzelius, and N. Gisin, "Approaches for a quantum memory at telecommunication wavelengths," *Phys. Rev. A* **83**, 012318– (2011).
 8. M. S. Shahriar, P. Kumar, and P. R. Hemmer, "Connecting processing-capable quantum memories over telecommunication links via quantum frequency conversion," *Journal of Physics B: Atomic, Molecular and Optical Physics* **45**, 124018– (2012).
 9. J. Huang and P. Kumar, "Observation of quantum frequency conversion," *Phys. Rev. Lett.* **68**, 2153–2156 (1992).
 10. S. Tanzilli, W. Tittel, M. Halder, O. Alibart, P. Baldi, N. Gisin, and H. Zbinden, "A photonic quantum information interface," *Nature* **437**, 116–120 (2005).
 11. M. T. Rakher, L. Ma, O. Slattery, X. Tang, and K. Srinivasan, "Quantum transduction of telecommunications-band single photons from a quantum dot by frequency upconversion," *Nat Photon* **4**, 786–791 (2010).
 12. S. Ates, I. Agha, A. Gulinatti, I. Rech, M. T. Rakher, A. Badolato, and K. Srinivasan, "Two-photon interference using background-free quantum frequency conversion of single photons emitted by an InAs quantum dot," *Phys. Rev. Lett.* **109**, 147405– (2012).
 13. Y. Ding and Z. Y. Ou, "Frequency downconversion for a quantum network," *Opt. Lett.* **35**, 2591–2593 (2010).
 14. N. Curtz, R. Thew, C. Simon, N. Gisin, and H. Zbinden, "Coherent frequency-down-conversion interface for quantum repeaters," *Opt. Express* **18**, 22099–22104 (2010).
 15. H. Takesue, "Single-photon frequency down-conversion experiment," *Phys. Rev. A* **82**, 013833– (2010).
 16. S. Zaske, A. Lenhard, and C. Becher, "Efficient frequency downconversion at the single photon level from the red spectral range to the telecommunications c-band," *Opt. Express* **19**, 12825–12836 (2011).
 17. S. Zaske, A. Lenhard, C. A. Keler, J. Kettler, C. Hepp, C. Arend, R. Albrecht, W.-M. Schulz, M. Jetter, P. Michler, and C. Becher, "Visible-to-telecom quantum frequency conversion of light from a single quantum emitter," *Phys. Rev. Lett.* **109**, 147404– (2012).
 18. K. De Greve, L. Yu, P. L. McMahon, J. S. Pelc, C. M. Natarajan, N. Y. Kim, E. Abe, S. Maier, C. Schneider, M. Kamp, S. Hofling, R. H. Hadfield, A. Forchel, M. M. Fejer, and Y. Yamamoto, "Quantum-dot spin-photon entanglement via frequency downconversion to telecom wavelength," *Nature* **491**, 421–425 (2012).
 19. R. Ikuta, Y. Kusaka, T. Kitano, H. Kato, T. Yamamoto, M. Koashi, and N. Imoto, "Wide-band quantum interface for visible-to-telecommunication wavelength conversion," *Nat Commun* **2**, 537– (2011).
 20. A. G. Radnaev, Y. O. Dudin, R. Zhao, H. H. Jen, S. D. Jenkins, A. Kuzmich, and T. A. B. Kennedy, "A quantum memory with telecom-wavelength conversion," *Nat Phys* **6**, 894–899 (2010).
 21. H. J. McGuinness, M. G. Raymer, C. J. McKinstrie, and S. Radic, "Quantum frequency translation of single-photon states in a photonic crystal fiber," *Phys. Rev. Lett.* **105**, 093604– (2010).
 22. D. Felinto, C. W. Chou, J. Laurat, E. W. Schomburg, H. de Riedmatten, and H. J. Kimble, "Conditional control of the quantum states of remote atomic memories for quantum networking," *Nat Phys* **2**, 844–848 (2006).
 23. C. Langrock, E. Diamanti, R. V. Roussev, Y. Yamamoto, M. M. Fejer, and H. Takesue, "Highly efficient single-photon detection at communication wavelengths by use of upconversion in reverse-proton-exchanged periodically poled LiNbO₃ waveguides," *Opt. Lett.* **30**, 1725–1727 (2005).
 24. J. S. Pelc, C. Langrock, Q. Zhang, and M. M. Fejer, "Influence of domain disorder on parametric noise in quasi-phase-matched quantum frequency converters," *Opt. Lett.* **35**, 2804–2806 (2010).
 25. M. A. Albota and F. C. Wong, "Efficient single-photon counting at 1.55 μm by means of frequency upconversion," *Opt. Lett.* **29**, 1449–1451 (2004).
 26. R. V. Roussev, C. Langrock, J. R. Kurz, and M. M. Fejer, "Periodically poled lithium niobate waveguide sum-frequency generator for efficient single-photon detection at communication wavelengths," *Opt. Lett.* **29**, 1518–1520 (2004).
 27. J. S. Pelc, C. Langrock, Q. Zhang, and M. M. Fejer, "Efficient down-conversion of single photons for quantum communication," in "OSA Technical Digest (CD)," (Optical Society of America, 2009), pp. NTuB1–.
 28. P. S. Kuo, J. S. Pelc, O. Slattery, Y.-S. Kim, M. M. Fejer, and X. Tang, "Reducing noise in single-photon-level frequency conversion," *Opt. Lett.* **38**, 1310–1312 (2013).
 29. J. S. Pelc, L. Ma, C. R. Phillips, Q. Zhang, C. Langrock, O. Slattery, X. Tang, and M. M. Fejer, "Long-wavelength-pumped upconversion single-photon detector at 1550nm: performance and noise analysis," *Opt. Express* **19**, 21445–21456 (2011).
 30. H. P. Specht, C. Nolleke, A. Reiserer, M. Uphoff, E. Figueroa, S. Ritter, and G. Rempe, "A single-atom quantum memory," *Nature* **473**, 190–193 (2011).
 31. M. Gündoğan, P. M. Ledingham, A. Almasi, M. Cristiani, and H. de Riedmatten, "Quantum storage of a photonic polarization qubit in a solid," *Phys. Rev. Lett.* **108**, 190504– (2012).
 32. S. Massar and S. Popescu, "Optimal extraction of information from finite quantum ensembles," *Phys. Rev. Lett.* **74**, 1259–1263 (1995).
 33. I. Marcikic, H. de Riedmatten, W. Tittel, H. Zbinden, and N. Gisin, "Long-distance teleportation of qubits at telecommunication wavelengths," *Nature* **421**, 509–513 (2003).
 34. F. Kaiser, A. Issautier, L. A. Ngah, O. Alibart, A. Martin, and S. Tanzilli, "A versatile source of polarization entangled photons for quantum network applications," *Laser Phys. Lett.* **10**, 045202 (2013).
 35. P. Palittapongarnpim, A. MacRae, and A. I. Lvovsky, "Note: A monolithic filter cavity for experiments in quantum optics," *Rev. Sci. Instrum.* **83**, 066101–3 (2012).
-

1. Introduction

Quantum repeaters [1–3] have been proposed as a potential solution to overcome the problem of exponential loss in optical fibers, that prevents the direct distribution of quantum information beyond a few hundred kilometers. Quantum repeaters rely on heralded entanglement between remote quantum memories (QMs) [2,3]. In absence of a heralding mechanism for the absorption of a photon in the QM, heralded entanglement is usually obtained by a measurement induced mechanism (e.g. a Bell state measurement) with light emitted by the remote QMs [2, 4, 5]. Despite initial work towards QMs operating in the telecom band [6, 7] most QMs operate in a wavelength range where the loss in optical fibers is significant. Hence a quantum interface allowing to connect these QMs to optical fibers by converting the emitted photons to telecom wavelengths is needed for almost all applications in the context of quantum communication [3, 8].

Quantum frequency conversion has attracted a lot of attention recently. Several nonlinear processes have been used, including frequency upconversion using sum frequency generation [9–12], frequency down conversion using difference frequency generation (DFG) [13–19] and four wave-mixing [20, 21]. DFG enables the conversion of visible or near infrared light to telecommunications wavelengths and is thus ideally suited for quantum repeater applications. The first proof of principle experiments of DFG at single photon level were reported in [14, 15]. Progress has been fast since this first demonstration, including high efficiency conversion [16] and conversion of non classical light emitted by single solid state emitters [17, 18] and by parametric down conversion sources [19]. However, most of the experiments done so far with DFG in nonlinear materials were done with very short pulses, not compatible with the narrow bandwidth of current emissive quantum memories, which typically emit transform limited single photon pulses with a few tens of ns duration [3, 22]. The realization of a narrowband, quantum memory compatible quantum frequency converter (QFC) is significantly more demanding in terms of noise suppression, as the duration of the converted photons is significantly longer than the single photon emitted by solid state emitters [12, 17, 18] and spontaneous down conversion sources [10, 19].

A proof of principle experiment of quantum frequency conversion from a Rubidium quantum memory to 1367nm has been reported recently, using four wave mixing in a cold and extremely dense atomic ensemble [20]. This technique, while efficient and noise free, requires a complex experimental setup and is restricted to wavelengths close to atomic transitions. In contrast, quantum frequency conversion based on nonlinear processes in $\chi^{(2)}$ or $\chi^{(3)}$ materials is more versatile, since it allows an almost free choice of the signal and converted wavelengths. This will be important in view of connecting quantum systems of different kinds. In addition the experimental setup is significantly simpler and can be integrated using waveguide technology.

In this paper, we report for the first time to our knowledge a photonic solid state quantum interface enabling the quantum frequency conversion of photons compatible with a Rubidium QM to telecommunication wavelengths. We use DFG in a periodically poled lithium niobate (PPLN) waveguide with a strong pump at 1569nm, to convert weak atom resonant coherent pulses of 30ns duration at the single photon level from 780nm to 1552nm. We show that the signal to noise ratio (SNR) is good enough to reduce the average input photon number μ_{in} below 1. In addition, we show that the noise decreases linearly with the spectral bandwidth of the device, suggesting that a narrower filtering should allow us to decrease the minimum input photon number required to achieve a $SNR > 1$. Finally, we measure the fidelity of the conversion process by using time-bin input qubits, and show that our device can operate with conditional fidelities higher than classical *measure and prepare* strategies taking into account the statistics of the input coherent states and the finite device efficiency.

The paper is organized as follows. The experimental setup is described in section 2. Section

3 is devoted to the characterization of the frequency conversion device, including a study of the efficiency of the process and of the related noise. In section 4, we report the experiments related to the phase preservation of the DFG process and finally in section 5 we discuss in more detail the performances of our device, and possible improvements.

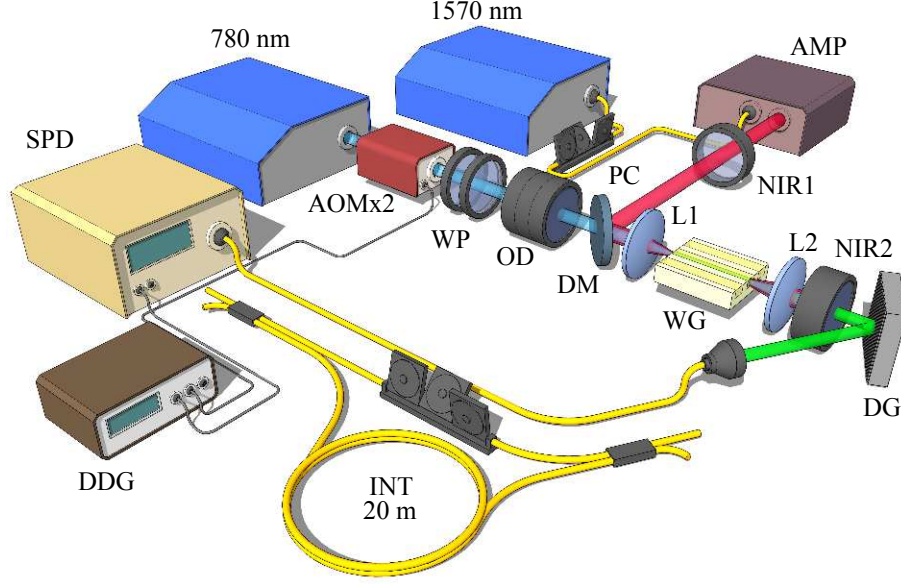


Fig. 1. Schematic view of the experimental setup. The pump laser is a diode at 1570 nm. PC: polarization controller. AMP: fiber amplifier. NIR1: band-pass filter to clean the ASE. The input light is obtained by a diode-tapered amplifier system at 780 nm. AOMx2: acousto-optic modulator in double passage. WP: half- and quarter- waveplates. OD: neutral density filters. The pump and input beams are overlapped on a dichroic mirror DM. L1: in-coupling lens. WG: non-linear waveguide. L2: out-coupling lens. NIR2: band-pass filter centered at 1552 nm plus long-pass filter with cut-off at 1450 nm. DG: diffraction grating. SPD: single photon detector. DDG: digital delay generator. INT: fiber interferometer.

2. Experimental setup

In the following section we will describe the main components of our frequency conversion unit. The experimental setup is schematically depicted in Fig. 1.

2.1. Laser sources

The pump light at $\lambda_p = 1569.4 \text{ nm}$ is provided by an external cavity diode laser (ECDL) amplified by a continuous wave Erbium doped fiber amplifier. In order to remove the amplified spontaneous emission (ASE) we use two bandpass filters centered at 1570 nm with a bandwidth of 9 nm (NIR1, Semrock). The peak transmission of the filters at 1569 nm is $> 98\%$, while around 1552 nm it is $< 10^{-5}$. The ASE is then suppressed by $> 100 \text{ dB}$ at the converted wavelength.

The input light at $\lambda_{in} = 780.24 \text{ nm}$ is obtained from a commercial system formed by an ECDL, followed by a tapered amplifier (Toptica TA pro). The laser is tuned to be resonant with the D_2 line of ^{87}Rb . In order to simulate photons obtained from a rubidium based quantum memory, about 20 mW of the total available power is sent through an acousto-optic modulator

(AOMx2) arranged in double passage configuration. Pulses are created with a full width half maximum (FWHM) of 30 ns, compatible with the 26.2 ns life time of the $5^2P_{3/2}$ excited state of ^{87}Rb and with durations of single photons emitted by quantum memories based on cold atomic ensembles [22]. A digital delay generator (DDG) is used to control the AOM and generate pulses at a repetition rate of 1 MHz. The input light is then fiber coupled (fiber not shown in Fig. 1) to clean its spatial mode. At the fiber output, a set of calibrated neutral density filters (OD) attenuate the laser intensity. The total optical depth given by the filters is measured to be 16.6(1). The mean photon number per pulse before the waveguide μ_{in} is then spanned from 0.3 to 25 by fine tuning of the laser power.

2.2. PPLN waveguide

The DFG process is based on Type 0 quasi phase-matching in a $L = 3$ cm periodically poled lithium niobate waveguide (5% MgO doped congruent PPLN, AR-coated for 780 and 1552–1569 nm, HC Photonics Corp.). The waveguide cross section of $7.08 \times 11.35 \mu\text{m}^2$ ensures single mode operation at 1552–1569 nm, while for the input light at 780 nm the propagation is multi-mode. The transmission losses specified by the manufacturer are 0.7 dB/cm (0.35 dB/cm) at 780 nm (1552 – 1569 nm). The waveguide is mounted on a copper holder, which is temperature stabilized by means of a Peltier unit used in combination with a home-made controller. The chip temperature is maintained around 320 K, to ensure quasi-phase matching and thus maximizing the conversion efficiency.

The pump light polarization is adjusted to be oriented along the proper crystal axis by means of a polarization controller (PC) placed between the seed laser and the amplifier. For the input light the polarization is adjusted with a combination of a half- and a quarter-waveplate (WP). The input and pump beams are overlapped on a dichroic mirror (DM) and coupled to the waveguide by means of an aspheric lens (L1) with focal length $f = 15.9$ mm and numerical aperture $NA = 0.16$. The in-coupling lens is mounted on an XYZ flexure stage for fine adjustment of the waveguide coupling. The converted light is then out-coupled by means of a second aspheric lens (L2) with the same focal length and numerical aperture as L1. The transmission at 1570 nm is measured to be higher than 98 %, while only 80 % of the input light is transmitted.

Table 1. Summary of the losses at the different elements.

Transmission	$\lambda_{in} = 780 \text{ nm}$	$\lambda_p = 1569 \text{ nm}$
Input lens (L1)	0.99	0.66
Waveguide (WG) coupling	0.61	0.58
Waveguide (WG) propagation	0.61	0.78
Output lens (L2)	0.80	0.98
Total	0.29	0.30

The transmission of the pump (input) light through the converter is measured to be 30 % (29 %). These values account for the coupling efficiency in the waveguide and the losses experienced during the propagation through the crystal as well as the coupling lenses. Using the transmission values specified above, we infer that the coupling efficiency of the pump (input) in the waveguide is 58 % (61 %). Table 1 summarizes the various losses in the waveguide and associated optics.

Note that the pump light attenuation does not present a significant problem, since the total available power is much higher than the value required to operate the experiment. On the other hand, the waveguide transmission at λ_{in} is a crucial parameter, since it affects the device efficiency and a lower transmission reduces the *SNR* for the converted photons. It is also important

to note that the transmission at 780 nm has been measured after optimizing the DFG signal with classical light. The fact that the waveguide is multimode at 780 nm and that the input and the pump modes have different mode diameters indicates that the maximum conversion efficiency does not necessarily corresponds to the maximum input coupling. The waveguide coupling at the input wavelength could be increased by using ridge waveguides for which it has been shown that coupling efficiencies up to 90 % can be achieved [16].

2.3. Filtering stage

A fundamental part of our setup is the filtering stage used to isolate the converted signal at $\lambda_{out} = 1552$ nm from the noise. In this type of quantum frequency conversion experiments two main contributions to the noise in the vicinity of λ_{out} can arise: leakage of the strong pump at 1569 nm and spontaneous Raman scattering [16, 23]. In our case spontaneous parametric down conversion (SPDC) of the pump photons [24] can not contribute to the noise, since $\lambda_{out} < \lambda_p$. It has also to be noted that light at 785 nm could be created by weakly phase matched second harmonic generation (SHG) of the strong pump.

In order to remove the unconverted input photons and the light created by SHG of the pump we use a long pass filter with cut-off wavelength of 1450 nm (Thorlabs), placed right after the waveguide. Its transmission at 1552 nm is $\sim 85\%$, while its optical depth in the 700 - 800 nm range is ~ 5 . The residual pump light is then blocked by means of two band-pass filters centered at 1552 nm with a bandwidth of 7 nm (Semrock, transmission $\sim 93\%$).

A diffraction grating (600 lines per mm, $1.6\mu\text{m}$ blaze, Thorlabs) is then used to map the frequency spectrum of the converted light into angular dispersion. The incidence angle of 3 deg has been chosen to increase the spectral resolution while maintaining a sufficient diffraction efficiency. The light diffracted in the first order is then coupled to a single mode fiber, thus selecting only a narrow spectral region. This method offers two advantages. On the one hand, narrower transmission bandwidths are achievable. On the other hand, this solution allows us to vary the filtering width up to a certain extent. This is achieved by changing the focal position of the out-coupling lens, thus modifying the aspect ratio of the converted beam at the position of the fiber coupler. When the beam is elongated in a direction perpendicular to the grating dispersion, the minimum filter bandwidth is achieved. When the aspect ratio is inverted, the filter resolution is reduced. This allows us to span the transmission bandwidth from 0.65 nm (80 GHz) to 2.3 nm (287 GHz).

The total transmission of the filtering stage at $\lambda_{out} = 1552$ nm is about 26%. This number accounts for the single mode fiber coupling ($\sim 50\%$), the diffraction grating efficiency (70%), and the transmission of the long-pass and band-pass filters (74%).

The converted photons are finally detected by means of a single photon detector (SPD, id201, idQuantique) operated in gated mode, with an overall detection efficiency of 7%, which includes the detector efficiency (10%) and a fiber to fiber connection (70%). The dark count probability is about 10^{-5} ns^{-1} . In order to avoid afterpulses we adopt a dead time of 20 μs . The photon counter is triggered by the DDG in order to synchronize the detection window with the photon arrival time.

3. Device characterization

In this section we will describe different measurements intended to characterize the device operation and efficiency.

3.1. Pulse width and detection window

As stated in the previous section, the input pulses are characterized by a wavelength of $\lambda_{in} = 780$ nm and a FWHM of 30 ns to mimic photons obtained from DLCZ quantum mem-

ories [22]. In order to verify their compatibility with Rubidium based atomic ensembles, we send weak input pulses to a cold cloud of ^{87}Rb atoms confined in a magneto-optical trap. This is part of another setup present in the same laboratory and used to implement an ensemble based QM. After interacting with the atomic ensemble, the light pulses are sent to the QFC and the corresponding 1552nm converted photons are detected. The transmission of the input photons through the atomic cloud as a function of the input frequency is plotted in Fig. 2(a). A typical absorption profile can be observed. The efficient absorption confirms that the input pulses interact strongly with the atoms. A fit to the experimental data gives a value for the full width at half maximum of the absorption peak of 16(1)MHz. This value is close to the convolution between the natural linewidth of the transition (6MHz) and the bandwidth of the close to Gaussian input photons ($0.44/(30\text{ns}) = 14\text{MHz}$).

We then measure the photon shape after the QFC, in order to verify that it is preserved during the conversion process. We prepare input pulses with a mean photon number $\mu_{in} = 5$ and send them to the converter. By means of the DDG, we trigger the photon counter such that the detection window of 100ns is centered around the photon arrival time. The counts given by the single photon detector are then acquired by a time stamping card (Signadyne) together with the trigger signal. We finally perform a start-stop measurement, using the trigger as start and a 1552nm detection as stop. The results are shown in Fig. 2(b). The detector dark counts per time-bin (dc) are obtained by blocking the waveguide input during the measurement (green dots). The noise level (n , including dark counts) is obtained in the presence of the pump light only, blocking the 780nm input (blue dots). The signal (s , including noise and dark counts) is plotted with red dots.

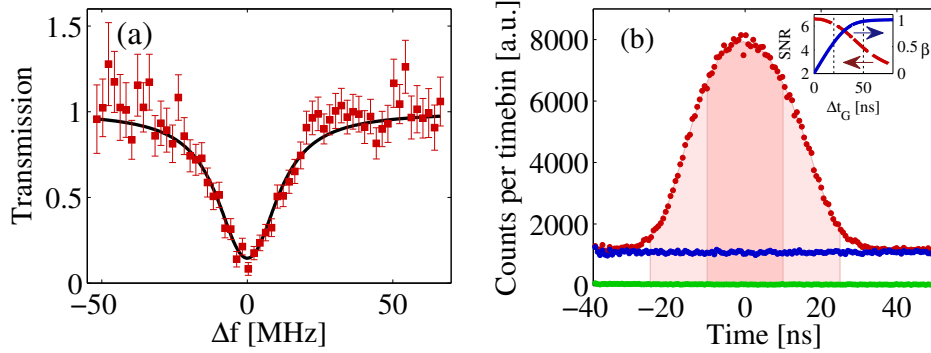


Fig. 2. **(a)** Transmission of weak input pulses through a cloud of cold ^{87}Rb atoms as a function of detuning. The probe light at 780nm is converted to 1552nm after interacting with the atomic cloud and then detected with the SPD. **(b)** Temporal shape of the converted photons. The time-bin was 0.64ns. The shaded areas represent the detector gates of 20 and 50ns. Inset: signal to noise ratio (left axis) and β factor (right axis) as a function of the detection window. The plot is obtained using the data points shown in the main figure (see text for details).

In a typical experiment, the detected counts are integrated over a certain time window characterized by a width Δt_G . In the following, we will refer to the total signal as $S = \int_{\Delta t_G} s dt$. Similar definitions are employed for the total noise (N) and dark counts (DC). Two figures of merit guide us in the choice of Δt_G : the detected signal fraction β and the signal to noise ratio SNR . β is defined as $(S - N)/(S' - N')$, where S' (N') is the signal (noise) for $\Delta t_G \rightarrow \infty$. The signal to noise ratio with dark counts subtracted is defined as $SNR = (S - N)/(N - DC)$. On the

one hand, β increases by extending the detection region, reaching the asymptotic value of 1 for $\Delta t_G \rightarrow \infty$. On the other hand, as Δt_G increases the SNR drops to 0, since the noise increases linearly with Δt_G , while the signal fast saturates to S' for $\Delta t_G > 30$ ns. This behavior is illustrated in the inset of Fig. 2(b).

The single photon detector we use allows only for certain detection window widths. The values closer to the pulse FWHM used in the experiments are 20 and 50 ns, represented as red shaded areas in Fig. 2(b). While $\Delta t_G = 50$ ns corresponds to the highest detected signal fraction ($\beta = 0.97$), $\Delta t_G = 20$ ns offers the highest SNR with $\beta = 0.57$. Unless otherwise specified, for the measurement described in the following we adopt a 20 ns detection window.

3.2. Noise vs pump power

The noise level N introduced in the previous section is related to the pump power P_p . We measured the noise as a function of P_p in absence of input signal, as shown in Fig. 3(a), and found that it follows a linear relation:

$$N(P_p) = \alpha \cdot P_p + DC, \quad (1)$$

This behavior suggests that the noise is originated either by pump leakage or by spontaneous Raman scattering. A fit of the experimental data gives $\alpha \sim 6 \times 10^{-6}$ /mW for $\Delta t_G = 20$ ns. This value expresses the noise level for detected events. If we back propagate to the crystal by correcting for optical losses (see section 3.3), we find that the noise floor is $\alpha' = 10^{-4}$ /mW for $\Delta t_G = 20$ ns. It is important to notice that this value is valid only for the filtering width of ~ 0.7 nm (85 GHz) used for the measurements discussed in the following.

The fact that the noise is linearly related to the pump power with a slope which has been properly calibrated, allows us to consider N as an indirect measurement of P_p . This technique simplifies the determination of the pump power and it has been used to obtain the quantity plotted in the horizontal axis of Fig. 3(b), discussed in the following section.

3.3. Conversion and total efficiencies

In order to measure the total efficiency, we send weak coherent pulses with $\mu_{in} = 6.1$ and we measure the probability to detect a photon per gate with (p_S) and without input pulse (p_N) as a function of the pump power, as shown in Fig. 3(a) [16]. The total efficiency, including all losses, is then calculated by $\eta_{tot} = (p_S - p_N) / \mu_{in}$.

We find a maximum total efficiency $\eta_{tot}^M = 2.6 \times 10^{-3}$. By correcting for the detection efficiency ($\eta_{det} = 0.07 \times \beta = 0.04$), we can infer the maximal device efficiency $\eta_{dev}^M = 0.066$, which can be interpreted as the probability to find a photon in a single mode fiber at the output of the conversion device (including spectral filtering) with $\mu_{in} = 1$. Finally, by correcting for the transmission of the filtering system (0.26) we can compute the external conversion efficiency of the waveguide, corresponding to $\eta_{ext} = \mu_{out} / \mu_{in}$ where μ_{out} is the average number of photons at 1552 nm at the output of the waveguide ($\eta_{ext}^M = 0.25$). η_{ext} is limited by the coupling into the waveguide ($\eta_c = 0.61$), so the maximal internal waveguide conversion efficiency is $\eta_{int}^M = 0.41$. The various efficiencies and losses are summarized in Table 2.

In Fig. 3(b), the external efficiency is plotted as a function of the pump power measured after the waveguide P_p (red dots, left axis). The continuous line is a fit of the experimental data with the formula:

$$\eta_{ext} = f(P_p) = \eta_{ext}^M \sin^2(L\sqrt{P_p \cdot \eta_n}), \quad (2)$$

where η_n is the normalized efficiency and L the waveguide length. This formula is obtained by treating the pump as a classical field and assuming that the converted photon input is in the vacuum state [23, 25–27]. We use η_{ext}^M and η_n as free parameters. We find $\eta_n \sim 72(7)\% / \text{W} \cdot \text{cm}^2$,

Table 2. Efficiency definitions and values. See text for details.

Description	Individual		Cumulative	
Coupling efficiency	η_c	0.61	η_{int}^M	0.41
Effective waveguide transmission	η_t	0.7	η_{ext}^M	0.25
Filter transmission	η_f	0.26	η_{dev}^M	0.066
Detection efficiency (incl. β)	η_d	0.04	η_{tot}^M	0.0026

which for our 3 cm long waveguide leads to a total normalized conversion efficiency of $\eta_c = 650(70)\%/\text{W}$.

As can be seen in the plot, the maximum conversion efficiency is achieved for $P_p \sim 400\text{ mW}$, corresponding to an input power before the waveguide $P_{in} = 1.33\text{ W}$, which is far below the maximum output power of our amplifier ($\sim 5\text{ W}$).

The maximal internal conversion efficiency should be 1 in theory. In practice, it is limited by internal waveguide losses. We have not measured them directly, but according to the specification of the manufacturer we can infer an effective transmission of $\eta_t \sim 0.7$, assuming that photons are created at the center of the waveguide. This would set the maximal achievable value for η_{int}^M . The remaining discrepancy between the inferred $\eta_{int}^M = 0.41$ and $\eta_t \sim 0.7$ could be explained by non perfect mode overlap and by variations of the poling period along the waveguide [16].

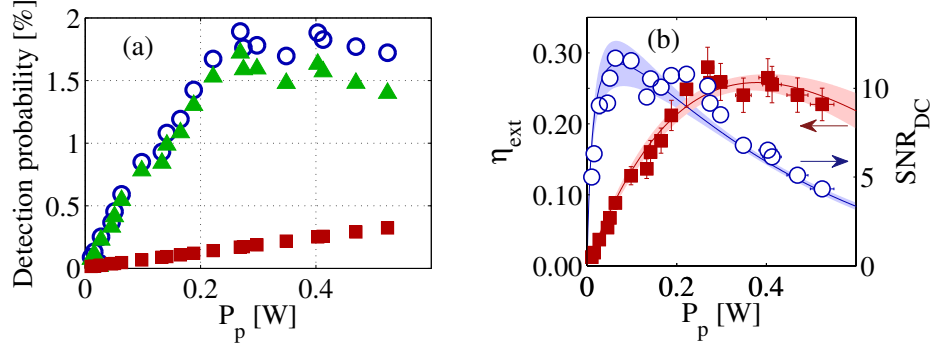


Fig. 3. **(a)** Detection probabilities with (p_S , blue open circles) and without (p_N , red squares) input signal ($\mu_{in} = 6.1$) as a function of the pump power P_p measured after the waveguide. The green triangles correspond to the pure signal ($p_S - p_N$). **(b)** External conversion efficiency (η_{ext}) as a function of P_p (red dots, left axis). The continuous line is a fit using Eq. (2). The red shaded area represents the 95% confidence interval of the fit. We observe a normalized conversion efficiency of $\eta_n = 650(70)\%/\text{W}$. On the right axis we show the signal to noise ratio. The experimental data (blue dots) are compared with Eq. (3), where all the parameters are determined independently. The blue shaded area accounts for the errors associated to the different quantities involved in Eq. (3).

3.4. Signal to noise ratio and pump power

As explained in section 3.1, another relevant figure of merit to analyze the conversion process is the signal to noise ratio (SNR). Combining Eqs. (1) and (2), and recalling the definitions of S

and η_{tot} , we can derive the following relation:

$$SNR_{DC}(P_p) = \frac{P_S - P_N}{P_N} = \frac{\mu_{in} \cdot \eta_{\text{tot}} \cdot f(P_p)}{\alpha \cdot P_p + DC}. \quad (3)$$

The subscript DC indicates that the signal to noise ratio is taken without dark count subtraction, since here we want to account for the limitations given by our detection system.

It has to be observed that the signal shows an oscillatory behavior as a function of the pump power, while the noise increases linearly. As a consequence, SNR_{DC} initially increases with P_p until it reaches a maximum and then decreases to zero. When dark counts are subtracted SNR shows a maximum at zero pump power and then decreases as P_p increases. This behavior can be seen in Fig. 3(b), where the measured SNR_{DC} is plotted as a function of the pump power (blue dots, right axis). The experimental data belongs to the same series analyzed in the previous section. The blue continuous line is obtained from Eq. (3) with no free parameter. All the values involved in the formula (η_{tot} , α , *etc.*) have been independently measured. The blue shaded area accounts for the experimental errors on these parameters. It is remarkable that the expected theoretical curve reasonably agrees with the measured data within the error bars.

As we observed in section 3.3, the pump power required to achieve maximum efficiency is about 400 mW. Under this condition, the measured signal to noise ratio is only half of its maximum value. On the other hand, at $P_p \sim 100$ mW the signal to noise ratio reaches its optimum for a conversion efficiency which is about half of η_{ext}^M . Since these two quantities cannot be varied independently, the pump power has to be chosen in order to find a tradeoff between efficiency and SNR_{DC} . For the measurements described in the following sections, we choose $P_p \sim 120$ mW.

3.5. Signal to noise ratio and filtering bandwidth

As detailed in section 3.2, the noise level detected in the experiment is linearly proportional to the pump power. We noticed that N cannot be significantly reduced by introducing an extra band-pass filter centered at 1552 nm, with a transmission of only 10^{-5} at 1569 nm. This observation indicates that the noise level is only weakly related to leakage of the pump, and suggests that it could be mainly due to spontaneous Raman scattering of the 1569 nm light. The spectrum of Raman scattering typically extends over a region of several hundreds of nanometers, and it could then have a significant contribution around the converted wavelength λ_{out} . If this is the case, we should observe a variation of the noise level related to a change in the filtering bandwidth $\Delta\lambda$.

In order to confirm this intuition, we proceed as follows. For a given value of $\Delta\lambda$ we measure the signal to noise ratio (SNR , with dark counts subtraction) for the converted photons as a function of the mean input photon number μ_{in} (see Fig. 4(b)). We measure then the quantity μ_1 , defined as the value of μ_{in} required to get $SNR = 1$. We repeat this measurement for different values of the filtering bandwidth and observe the dependence of μ_1 as a function of $\Delta\lambda$. Assuming a constant level of Raman noise in the vicinity of λ_{out} , the noise level is expected to be proportional to the bandwidth of the filtering stage.

As we observed in section 2.3, the filtering bandwidth can be varied by moving the out-coupling lens L2 along its axis. For each position of L2, we measure the transmission of the filtering stage as a function of wavelength which allows us to determine the filtering bandwidth $\Delta\lambda$. To perform this measurement, we replace the pump laser with a tunable laser source (Tunics Plus, from Photonics) and scan its wavelength while monitoring the transmitted power through the filtering stage. A typical curve is shown in Fig. 4(c). Note that, since the system is aligned to maximize the total transmission, it may happen that the maximal transmission of the grating T_{max} is at a wavelength slightly different from λ_{out} . However, the transmission at λ_{out}

stands always above 90 % of T_{max} .

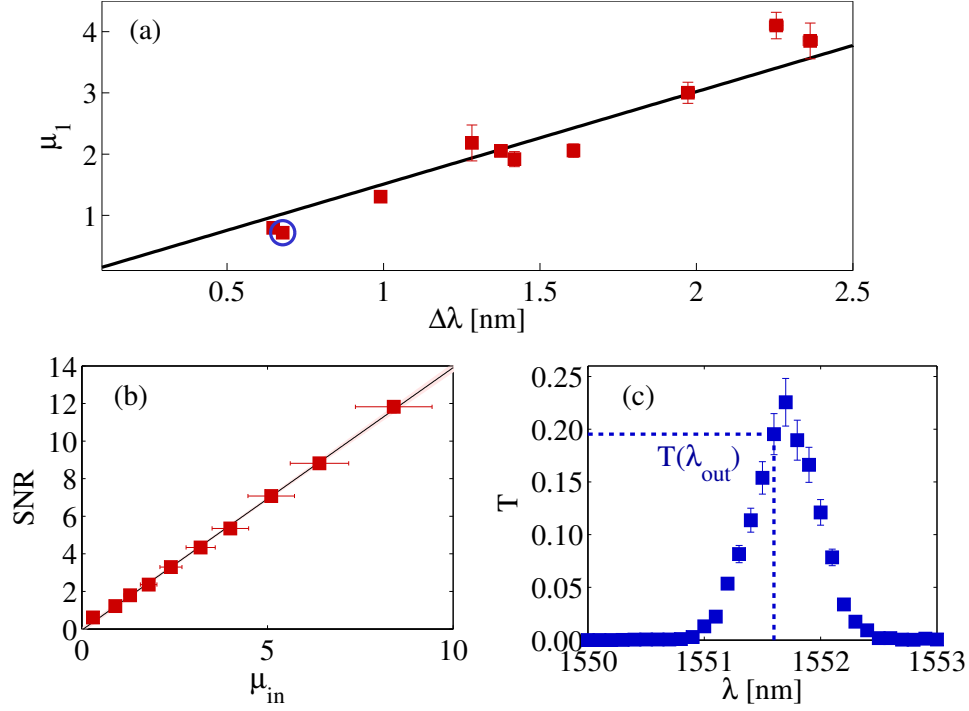


Fig. 4. **(a)** The mean number of photons in the input pulse required to achieve a SNR = 1 (μ_1) is plotted as a function of the filter width ($\Delta\lambda$). The solid line is a linear fit with no offset. **(b)** Signal to noise ratio as a function of the mean input photon number. The data shown correspond to the point highlighted with a blue circle in (a). In this case $\mu_1 = 0.7 \pm 0.1$. **(c)** Transmission of the filtering stage as a function of wavelength for the data points shown in (b). Here the linewidth is $\Delta\lambda = 0.68 \pm 0.01$ nm. The vertical dotted line indicates the target wavelength $\lambda_{out} = 1551.6$ nm. In this case the filter transmission at λ_{out} is $T(\lambda_{out}) = 0.23 \pm 0.01$.

In Fig. 4(a) we plot μ_1 as a function of $\Delta\lambda$. The solid line is a linear fit with no offset. The data points are in good agreement with the linear fit, which confirms that the noise is proportional to the filtering width, at least in this bandwidth range. For $\Delta\lambda = 0.68$ nm (~ 85 GHz), we observe $\mu_1 \sim 0.7 < 1$. This measurement allows us to conclude that the main source of noise for our setup has a broadband nature in the spectral region explored in the experiment. This suggests that the noise level could be significantly reduced by using a narrower filter (see section 5). Similar results have been recently achieved by Kuo et al. [28]. Together with previous observations, this also suggests that the noise is induced by spontaneous Raman scattering of the pump light. However, in order to unambiguously confirm that this is the case, a more detailed study would be required (see [16, 23, 29]).

4. Coherence preservation

In order to be used as a quantum interface, it is important to demonstrate not only that the device operates in the low noise regime, but also that the conversion is done in a coherent fashion [13]

and preserves the quantum superposition of an incoming qubit [14, 15]. To test the preservation of quantum coherence we perform an interference experiment with a pair of input pulses with a time difference of $\tau = 100$ ns, and a phase difference ϕ . This state can be seen as a time-bin qubit and can be written as $|\psi\rangle_{in} = |e\rangle + e^{i\phi}|l\rangle$ where $|e\rangle$ and $|l\rangle$ represent the early and late time-bins, respectively.

A fiber based interferometer is placed before the single photon detector in order to measure the coherence of the time-bin qubit (see Fig. 1). The interferometer is realized combining two 50-50 fiber beam splitters. In order to adjust the relative polarization between the two paths, a polarization controller is inserted in the short arm, while a 20 m single mode fiber in the long arm ensures a time delay of ≈ 100 ns between the two paths. The relative path length is not actively stabilized, but the interferometer is kept inside a polystyrene box to passively improve its temperature stability. The visibility of the interference fringes for classical light at 1569 nm is measured to be $\sim 96\%$, limited in part by the seed laser linewidth of 500 kHz. Note that, when performing interference with the converted photons, the linewidth of the input laser should also be taken into account.

If the travel time difference between the two arms of the interferometer corresponds to the time difference between the two input pulses τ , the pulses can exit the interferometers in three different time slots. The first and the last times slots corresponds to events $|e, S\rangle$ and $|l, L\rangle$, respectively, where S and L denote the short and long arms of the interferometer. The central time corresponds to two indistinguishable processes that can interfere: $|e, L\rangle$ and $|l, S\rangle$. The count rate in this time slot displays an interference as a function of the relative phase $(\phi - \gamma)$, where γ is the phase introduced by the interferometer. The visibility V of this interference fringe is a measure of the coherence preservation. To measure the visibility, we record counts in the central time slots as a function of the phase γ , for a pump power of 130 mW.

Figure 5(a) shows a measurement of the visibility of the interference fringes as a function of the average input photon number per pulse μ_{in} , for two different detection gate widths, $\Delta t_G = 20$ ns (plain squares) and $\Delta t_G = 50$ ns (open circles). Note that the visibilities displayed here are corrected for the maximal visibility of the interferometer $V_{max} = 0.96$. For high values of μ_{in} , we observe high visibilities $V > 0.9$, suggesting that the conversion process preserves the coherence to a great extent. However, the visibility decreases when decreasing μ_{in} as a result of a decrease of SNR . We also observe higher visibility for $\Delta t_G = 20$ ns, which is consistent with the fact that the decrease of visibility is due to higher noise level. To further confirm this hypothesis, the data are fitted with a model taking into account the SNR to determine the visibility:

$$V = V_0 \frac{\mu_{in}}{\mu_{in} + \mu_1/2}. \quad (4)$$

We observe an excellent agreement between this simple theoretical model and the experimental data.

Even if the light used to characterize the phase preservation is classical, it has been shown that it is possible to obtain information about the quantum character of the conversion [30, 31]. The idea is to measure the conditional (i.e. conditioned on a successful conversion of the qubit) fidelity F_c of the output qubit with respect to the input qubit and the compare the values obtained experimentally with the best obtainable fidelity using classical strategies. The conditional fidelity is defined as $F_c = \langle \psi_{in} | \rho_{out} | \psi_{in} \rangle$, where ρ_{out} is the density matrix of the output qubit and $|\psi_{in}\rangle$ is the state of the input qubit. It has been shown that if the qubits are encoded in Fock states, the classical strategy that maximize the fidelity is a "measure and prepare strategy", where the qubit is measured in some basis and a new qubit is prepared according to the measurement result [32]. For single photon qubits, this gives a classical fidelity of $2/3$. For qubits encoded in weak coherent states, as it is the case in our experiment, it is necessary to

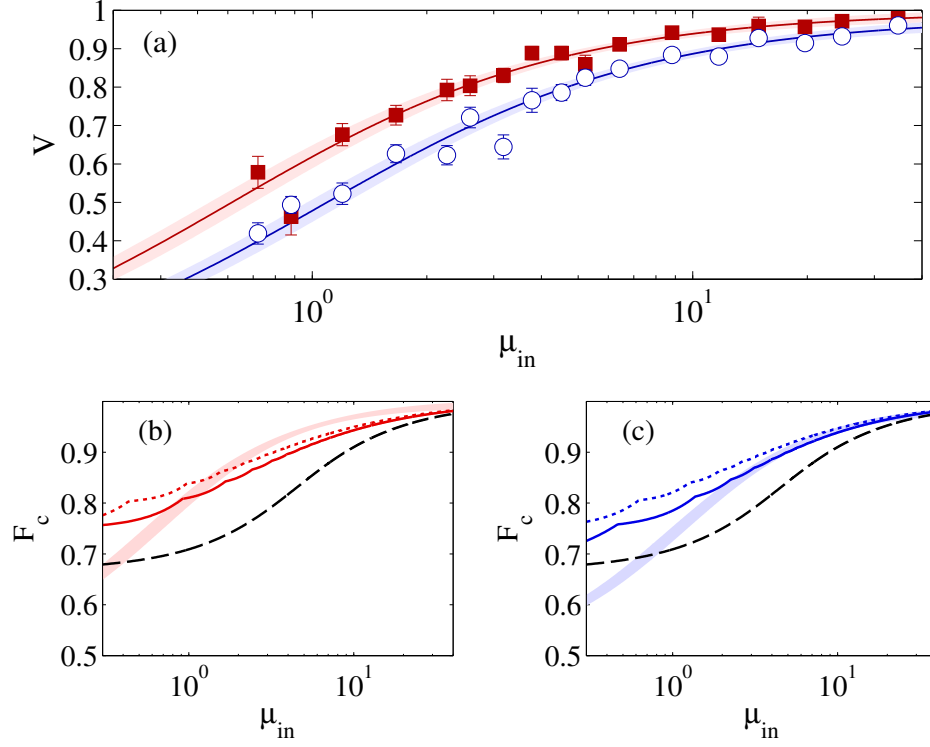


Fig. 5. **(a)** Visibility of the interference fringes as a function of μ_{in} for $\Delta t_G = 20$ ns (red plain squares) and $\Delta t_G = 50$ ns (blue open circles). The pump power is 130 mW. The visibilities are corrected for the maximal visibility of the interferometer $V_{max} = 0.96$. The solid lines are fits with Eq. (4) and the shaded areas represent the 95% confidence interval of the fits. **(b)** Comparison between experimental fidelities measured for $\Delta t_G = 20$ ns (shaded area taken from (a)) and the best achievable fidelities using a classical *measure and prepare* strategy. The dashed line corresponds to $\eta = 1$, the solid line to the external efficiency $\eta_{ext} = 0.10$ and the dotted line to device efficiency $\eta_{dev} = 0.025$ inferred for these measurements. **(c)** Same as (b) but for $\Delta t_G = 50$ ns. The solid line corresponds to $\eta_{ext} = 0.21$ and the dotted line to device efficiency $\eta_{dev} = 0.055$.

take into account the Poissonian statistics of the input light field and the finite efficiency of the quantum frequency conversion device, as shown in [30, 31]. Under these conditions, the maximal classical fidelity increases with the average input photon number μ_{in} .

For superposition states F_c can be obtained from the visibility V from the relation $F_c = (1 + V)/2$ [33]. Note that we should in principle take into account an average fidelity including the fidelities for the basis states $|e\rangle$ and $|l\rangle$. However, we assume here that these fidelities are higher than the ones for superposition states, which is justified by the fact that there is no coherence involved. Figures 5(b) and 5(c) show the comparison between the best classical strategies and the experimental results (shaded area) for $\Delta t_G = 20$ ns and $\Delta t_G = 50$ ns, respectively. The different lines correspond to different efficiencies. The dashed line corresponds to $\eta = 1$, i.e. takes only into account the Poissonian statistics of the input fields. The solid (dotted) line corresponds to the external conversion (device) efficiency inferred for that experiment. For $\Delta t_G = 20$ ns, we have $\eta_{ext} = 0.11$ and $\eta_{dev} = 0.028$ while for $\Delta t_G = 50$ ns, we have $\eta_{ext} = 0.21$ and $\eta_{dev} = 0.055$. The difference between the values for $\Delta t_G = 20$ ns or 50 ns is mostly due to the fact that in this case we do not correct for the β factor in the detection efficiency during the backpropagation, since the noise is measured for a given gate width. As can be seen in the figures, the best classical fidelities increase when decreasing the efficiency, as explained in [30, 31]. We observe that for $\Delta t_G = 20$ ns, the measured fidelities are higher than the classical threshold for μ_{in} between 2 and 25 in all cases. For $\Delta t_G = 50$ ns, the device is at the limit of operating in the quantum regime, when considering $\eta_{ext} = 0.21$.

5. Discussion

We have shown that the noise can be reduced sufficiently to operate the frequency converter with single photon level input fields compatible with atomic quantum memories. However, in order to use this device with single photon fields emitted by the atomic memory, a significant reduction of noise is needed to compensate for the finite retrieval efficiency of the memory and passive losses between the memory and the converter. The measurement of the SNR vs filter bandwidth suggests that the noise is broadband, and inversely proportional to the filter bandwidth. Since our input photons are relatively long (30 ns FWHM), the filter bandwidth could be ideally reduced down to ~ 50 MHz, thus decreasing significantly the noise and only weakly affecting the signal transmission (96 % transmission for a gaussian filter). In Section 3.2, we have inferred an unconditional noise floor after the crystal of $\alpha' = 5 \times 10^{-6} \text{ mW}^{-1} \text{ ns}^{-1}$ for a filter linewidth of 85 GHz. From this value, and assuming a linear scaling down to the MHz level, we infer that for a 50 MHz bandwidth we should obtain $\alpha' \sim 3 \times 10^{-9} \text{ mW}^{-1} \text{ ns}^{-1}$. This would lead to an unconditional noise floor of 6×10^{-5} photons at the maximum conversion efficiency and for $\Delta t_G = 50$ ns. This number is only given to infer the final limitation of our device. Further measurements should be performed to confirm the validity of the linear behavior to much narrower bandwidth. In order to reach this narrow bandwidth, phase shifted Fiber Bragg grating [34] or Fabry-Perot cavity could be used. It is likely that such narrow filter would have to be actively stabilized with respect to the converted light frequency. This may result in significant increase of the technical complexity of the setup and it could potentially introduce additional noise in the system. However, recent results on the experimental realization of medium finesse (~ 200) monolithic resonators [35] suggest that a narrower filtering could be achieved without a substantial increase of the setup complexity. A significant noise reduction could already be achieved with a fiber Bragg grating filter with 1 – 2 GHz bandwidth and passive thermal stability, leading to an inferred $\mu_1 < 0.02$. This should be sufficient to obtain high SNR with single photon input and realistic memory retrieval efficiencies.

6. Conclusion

We have presented a photonic quantum interface capable of converting weak atomic resonant light to telecommunication wavelength. We showed that weak coherent states with $\mu_{in} < 1$ with a duration of 30 ns can be converted from 780 nm to 1552 nm and detected with a signal to noise ratio above 1. We showed that the conversion process preserves the coherence of time-bin input qubits and that the device can operate in the quantum regime. We revealed the broadband nature of our main source of noise and have measured an unconditional noise floor after the crystal of 5×10^{-6} photons per mW of pump power and per nanosecond, for a filter spectral bandwidth of 85 GHz. In addition, we showed that the noise level can be controlled tuning the bandwidth of the filtering stage. This suggests that much lower noise level can be reached using narrower filters. This could lead to an unconditional noise floor sufficiently low to enable practical frequency conversion of non classical light emitted from atomic quantum memories using an integrated waveguide device.

Acknowledgments

We acknowledge financial support by the ERC starting grant QuLIMA and by the Spanish MINECO (project FIS2012-37569). We thank Valerio Pruneri, Davide Janner and Vittoria Finazzi for lending us the tunable laser at 1550 nm and for stimulating discussions.